Scholars Journal of Engineering and Technology
Abbreviated Key Title: Sch J Eng Tech
ISSN 2347-9523 (Print) | ISSN 2321-435X (Online)
Journal homepage: https://saspublishers.com

OPEN ACCESS

DFT Study of Optoelectronic and Thermoelectric Properties of Halide Double Perovskite Rb_2TlSbX_6 (X = Cl, Br, I) for Solar Cell Applications

Mehwish Nazar[1], Muhammad Naeem Tabassam[2], Aqidat Irfan[3], Maryam Liaqat[4], Muqaddas Ameen[5], Hamid Mehmood Chaudhary[6], Kashif Murad[7], Safder Alam[8], Muhammad Sohaib[9], Waheed Zaman Khan[10]*

[1]School of Science, Department of Chemistry, University of Management and Technology, Lahore 42000, Pakistan
[2]College of Physics and Optoelectronics Engineering, Shenzhen University, Shenzhen 518060, China
[3]Department of Physics, University of Agriculture, Faisalabad 38000, Punjab, Pakistan
[4]College of Electronics and Information Engineering, Shenzhen University, Shenzhen 518060, China
[5]Centre of Excellence in Solid State Physics, University of the Punjab, Lahore-54590, Pakistan
[6]Department of Physics, National University of Sciences and Technology (NUST), Islamabad, Pakistan
[7]Faculty of Mechanical Engineering, Ghulam Ishaq Khan Institute of Engineering Sciences and Technology, 23640, Khyber Pakhtunkhwa, Pakistan
[8]Department of Chemistry, Islamia College University of Peshawar, KPK, 25120, Pakistan
[9]School of Chemistry, Minhaj University Lahore 42000, Punjab, Pakistan
[10]Department of Physics, Division of Science and Technology, University of Education, Lahore, Punjab 54770, Pakistan

DOI: https://doi.org/10.36347/sjet.2025.v13i04.002 | **Received:** 25.02.2025 | **Accepted:** 04.04.2025 | **Published:** 08.04.2025

***Corresponding author:** Waheed Zaman Khan
Department of Physics, Division of Science and Technology, University of Education, Lahore, Punjab 54770, Pakistan

Abstract

Original Research Article

In this work, Rb_2TlSbX_6 with X = Cl, Br, or I will be studied using density functional theory (DFT) and BoltzTraP2 to investigate its structural, electronic, mechanical, optical, and thermoelectric properties. Analysis of the phonon dispersion confirms dynamic stability, while the absence of imaginary frequencies guarantees thermodynamic stability. Calculations of electronic band structures show that direct band gaps exist for each material, with $Rb_2TlSbCl_6$ having the most significant and Rb_2TlSbI_6 having the smallest due to the decreasing electronegativity of the halide ions. The total and partial density of states (TDOS and PDOS) indicate that dominant hybridisation between cations and anions results in a higher degree of carrier mobility. Strong light absorption in the visible to ultraviolet regions suggests these materials have high potential for photovoltaic and optoelectronic applications. Other estimated optical properties, such as the dielectric function, absorptivity coefficient, and refractive index, were found to support this claim. Stability assessments based on elastic constants reveal robust but ductile behavior. The thermoelectric characteristics exhibit notable Seebeck coefficients, power factors, and figure of merit (ZT), achieving a value of 1.99 at a temperature of 700 K. Their thermoelectric performance is further enhanced by a reduction in lattice thermal conductivity and a high BoltzTraP2 output. In general, Rb_2TlSbX_6 perovskites offer remarkable prospects for next-generation thermoelectric and photovoltaic devices due to their high energy conversion efficiency and ecological friendliness. Additional experimental work can help make them pivotal in the context of sustainable energy technologies.

Keywords: Lead-free perovskites, Rb_2TlSbX_6, Optoelectronic Properties, Thermoelectric Materials, DFT, BoltzTraP2.

INTRODUCTION

The potential of cost-effective photovoltaic devices has gained significant recognition in the scientific community with the development of Perovskite solar cells, which have an efficiency exceeding 25%. This surpasses the former, 2009 benchmark of 'first reported perovskite solar cells' and now competes with silicon-based solar cells. As researchers refine their parameters and optimise the perovskite materials, it is likely to result in higher efficiency levels downstream. Looking into other perovskite materials, lead-free double perovskites ($A_2BB'X_6$) marked new heights for the upcoming generation of solar cells. These innovations were introduced into the solar cell industry due to the distinct

Citation: Mehwish Nazar *et al*. DFT Study of Optoelectronic and Thermoelectric Properties of Halide Double Perovskite Rb□TlSbX□ (X = Cl, Br, I) for Solar Cell Applications. Sch J Eng Tech, 2025 Apr 13(4): 208-222.

structural features of traditional perovskites and their two other metal cations (B and B'). Not only do double perovskites enhance flexibility in composition, but they also prove beneficial for photovoltaic and optoelectronic applications. This paradigm shift has resulted in power conversion efficiencies exceeding 14% for Double Perovskite solar cells and considerably improved stability against environmental degradation factors, including moisture, heat, and light, compared to conventional lead-based perovskites [1, 2]. The mitigation of defect formation and enhanced lattice stability, provided by the two metal cations, gives double perovskites an unmatched standing in long-term performance.

The variety of B^+/B^{3+} cations in $A_2B^{3+}BX_6$ halide double perovskites provides Pb-based perovskites with potentially non-toxic alternatives. Some of the candidates investigated both theoretically and experimentally include Cs_2SnI_6 [3], Cs_2AgBiX_6 (X = Br, Cl) [2], $Cs_2InAgCl_6$ [4], $Cs_2InSbCl_6$, $Cs_2InBiCl_6$, $Rb_2CuInCl_6$, $Rb_2AgInBr_6$ and others. While these materials have specific promising properties, their band structures are not always optimal for solar energy applications. For instance, Cs_2AgBiX_6 (X = Br, Cl) exhibits excellent environmental stability, but its bandgap is indirect, which is detrimental to photovoltaic performance. On the other hand, Cs_2AgInX_6 (X = F, Cl, Br, I), studied by Tariq *et al.*, [5], was determined to possess a direct bandgap in the range of 3.44 eV to 0.7 eV, making it very advantageous for solar cells. Cs_2AgInI_6 from this family has been reported to have high thermoelectric power. Moreover, Dar *et al.*, [6], reported a double perovskite, Ba_2InTaO_6, with a Fm3m cubic structure, a lattice parameter of 8.28 Å, and semiconducting behavior. Numerous other double perovskite materials have also been studied for their potential applications in photovoltaic devices [7–10].

Aside from photovoltaics, the development of thermoelectric (TE) materials has been gaining attention due to their effective capabilities for recovering waste heat. Thermoelectric materials tend to be more applicable to narrow bandgap materials [11]. Bhandari *et al.*, [12], reported recently that $Ca_2Cr_{1-x}Ni_xOsO_6$ contains narrow bandgaps and shows promising values of thermoelectric efficiency. Moreover, Raihan *et al.*, thermally analysed the lead-free Ca_2MAsO_6 (M = Ga, In). They reported bandgap values of 2.61 eV and 2.83 eV, alongside a Seebeck coefficient that surpassed the threshold value posited by Hong *et al.*, [13], of 277 μV/K. Jitendra *et al.*, [14] also reported on the double perovskite Ra_2LaNbO_6, which shows an indirect bandgap of 2.4 eV and possesses significant potential for both photovoltaic and thermoelectric functionalities. Additionally, $(CH_3NH_3)_2AgInCl_6$, which is classified as an organometallic double perovskite, was said to exhibit significant efficiency for thermoelectric purposes with a reported ZT of 2.23 at 300 K for p-type doping [15].

While considerable progress has been made, the development of highly effective thermoelectric materials that function at room temperature remains a challenge [16–20]. This work aims to investigate the structural, electronic, mechanical, optoelectronic, and thermoelectric properties of Rb_2TlSbX_6 (X = Cl, Br, I), motivated by the performance of double perovskites. To the best of our knowledge, no previous studies have been conducted on these compounds, considering their potential applications in optoelectronics and thermoelectrics. Our findings show that these materials not only have narrow direct band gaps but are also likely to have values comparable to those of Cs_2AgTlX_6 (X = Br, Cl) [11], making them ideal candidates for solar cells and thermoelectric devices.

COMPUTATIONAL METHOD

Density Functional Theory (DFT) calculations for Rb_2TlSbX_6 (X = Cl, Br, I) were performed using the full-potential (FP) linearised augmented plane wave (LAPW+lo) method, as implemented in the WIEN2k package [21]. To determine optimised lattice parameters, ground-state energies, and structural and mechanical properties, the Perdew–Burke–Ernzerhof solids (PBEsol) functional within the generalised gradient approximation (GGA) was used for the exchange-correlation potential [22, 23]. The computational parameters included 1000 k-points, a cutoff energy of -9.0 Ry, a maximum angular momentum (lmax) of 10, a Gmax of 12, an RKmax of 8, and convergence thresholds of 0.00001 Ry for energy and 0.0001 eV for charge. The Phonopy code was employed to calculate the phonon dispersion curve using a 2 × 2 × 2 supercell with a 5 × 5 × 5 k-point mesh [24]. The electronic band structure was computed using the Tran-Blaha modified Becke-Johnson (TB-mBJ) potential, known for improving bandgap accuracy in semiconductors. The IRelast package was utilised to calculate the elastic constants. Optoelectronic properties were also evaluated using the TB-mBJ potential [25–27], while thermoelectric properties were computed with the BoltzTraP2 code [28]. Furthermore, the Phono3py code was used to determine lattice thermal conductivity, employing a 2 × 2 × 2 supercell with a 3 × 3 × 3 k-point mesh [29].

RESULTS AND DISCUSSION

a) Structural Properties

The unit cell of the cubic perovskite composition $Rb_2TlSbCl_6$ is depicted in Fig. 1. This structure crystallises in the Fm-3m (225) space group [30]. To determine the stable state and optimised structural parameters, we computed the total energy as a function of volume by applying a least-squares fit using the Birch-Murnaghan equation of state:

$$E(V) = E_0 + \frac{9B_0V_0}{16}\left[\left(\frac{V_0}{V}\right)^2 - 1\right]B_0' + \left(\frac{V_0}{V}\right)^2 - 1\left(6 - 4\left(\frac{V - V_0}{V}\right)^{\frac{3}{2}}\right)$$

The structure was optimised using the atomic Wyckoff positions A (0.25, 0.25, 0.25), (0.5, 0, 0), and (0, 0, 0), as well as X (x, 0, 0) [10]. The volume versus ground-state energy plots are shown in Figs. 2(a)–(c). The obtained values for these study materials are listed in Table 1. The lattice constant values increase with the replacement of halogens from Cl to I due to an increase in the atomic size of the anion. The results show consistency with other reported double perovskite materials. Moreover, the obtained values have similar lattice constants to Rb_2 $NaBiCl_6$ and K_2 $NaBiCl_6$ [7].

We checked the structural stability of our titled compounds through the octahedral, tolerance, and modified tolerance factors. These factors are calculated with the help of their ionic radii and the following relations [31-33]:

$$\tau = \frac{r_{\mathrm{Rb}} + r_X}{2\left(r_{\mathrm{Tl,Sb}} + r_X\right)}$$

$$\tau' = \frac{r_X}{r_{\mathrm{Tl,Sb}}} - n_{\mathrm{Rb}}\left[n_{\mathrm{Rb}} - \frac{\ln\left(r_{\mathrm{Rb}}/r_{\mathrm{Tl,Sb}}\right)}{\left(r_{\mathrm{Rb}}/r_{\mathrm{Tl,Sb}}\right)}\right]$$

$$\mu = \frac{r_{\mathrm{Tl,Sb}}}{r_X}$$

Additionally, the formation energy (ΔHf) was determined using:

$$\Delta H_f = E_{\mathrm{total}}(Rb^2TlSbCl^6) - 2E_{\mathrm{Rb}} - E_{\mathrm{Tl}} - E_{\mathrm{Sb}} - 6E_X$$

Where E_{total} is the total energy of the compound, and E_{Rb}, E_{Tl}, E_{Sb}, and E_{XE} are the energies of the constituent elements.

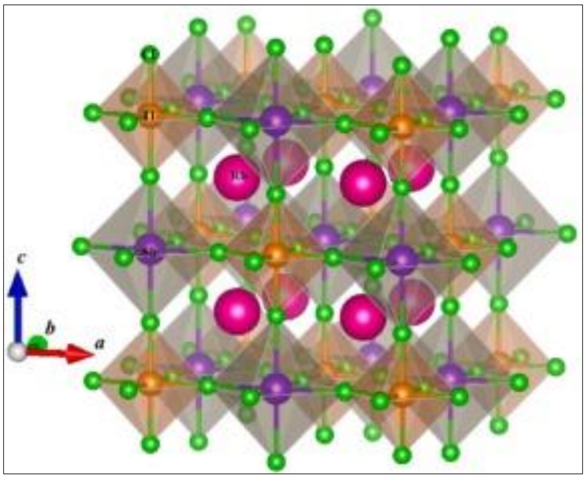

Fig. 1: The crystallographic structure of $Rb_2TlSbCl_6$.

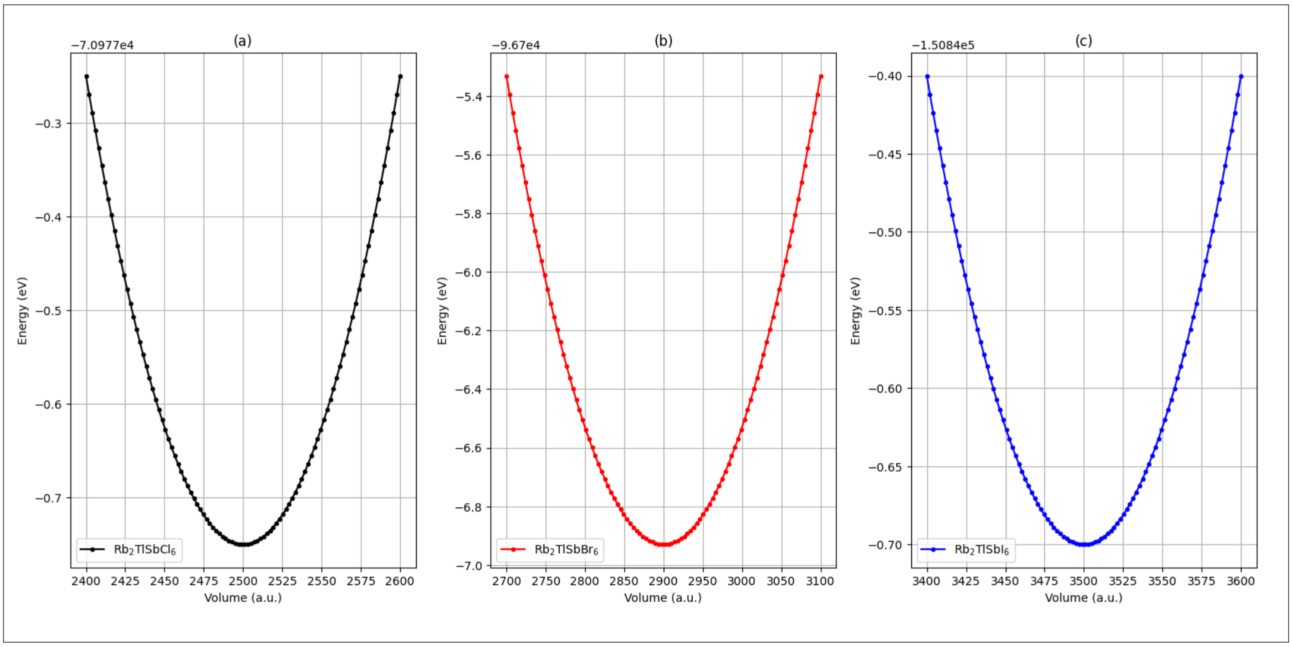

Fig. 2. The obtained optimised curve of (a) $Rb_2TlSbCl_6$, (b) $Rb_2TlSbBr_6$ and (c) Rb_2TlSbI_6

b) Structural Stability of Rb_2TlSbX_6 (X = Cl, Br, I) Compounds

This research presents a detailed investigation into the structural stability of Rb_2TlSbX_6 (X = Cl, Br, I) compounds, with a focus on their thermodynamic and dynamic stability. The computed structural parameters are summarised in Table 1, demonstrating the variations in lattice constant (a_0), formation energy (ΔHf), tolerance factor (τ), octahedral factor (μ), and tg values across the different halides.

Table 1: Computed Structural Parameters for Rb_2TlSbX_6 (X = Cl, Br, I) Compounds

Compounds	**$Rb_2TlSbCl_6$**	**$Rb_2TlSbBr_6$**	**Rb_2TlSbI_6**
a_0 (Å)	11.3877	11.9511	12.7627
ΔHf (eV)	−2.09	−1.74	−1.23
Tg	0.93	0.94	0.93
μ	1.15	1.21	1.07
T	2.91	2.89	2.95

The estimated negative values of formation energies indicated the thermodynamic stability of the titled compounds, as shown in Table 1. The higher formation energy (ΔHf = −2.09 eV) for $Rb_2TlSbCl_6$ indicates its more excellent stability compared to $Rb_2TlSbBr_6$ (−1.74 eV) and Rb_2TlSbI_6 (−1.23 eV).

The formation energy of Rb_2TlSbX_6 (X = Cl, Br, I) is also significantly higher than several previously reported perovskites, including C_2SeCl_6, Cs_2SnCl_6, K_2MnCl_6, and K_2OsCl_6, suggesting that the studied materials are more stable than many known double perovskites [34].

Beyond the formation energy, we also calculated the formation energy of its competing phase:
$TlX+RbTlX_2+Rb_3Sb_2X_9$ (X=Cl, Br, I)

The computed values for the competing phases are:

- **Cl-based** phase: **−1.81 eV/atom**
- **Br-based** phase: **−1.65 eV/atom**
- **I-based** phase: **−1.15 eV/atom**

These results indicate that the pristine Rb_2TlSbX_6 phase is more thermodynamically favorable than its competing phases for all halogens (Cl, Br, I). To further verify the stability of these compounds, phonon dispersion curves were computed along high-symmetry directions of the Brillouin zone. The obtained phonon dispersion relations for Rb_2TlSbX_6 (X = Cl, Br, I) are plotted in Fig. 3.

As shown in Fig. 3, there are no imaginary phonon modes observed for any of the three compounds throughout the Brillouin zone. The absence of imaginary frequencies strongly confirms the dynamical stability of the synthesised materials. This suggests that Rb_2TlSbX_6 double perovskites are structurally stable and can be synthesised experimentally for potential optoelectronic and energy-related applications [35].

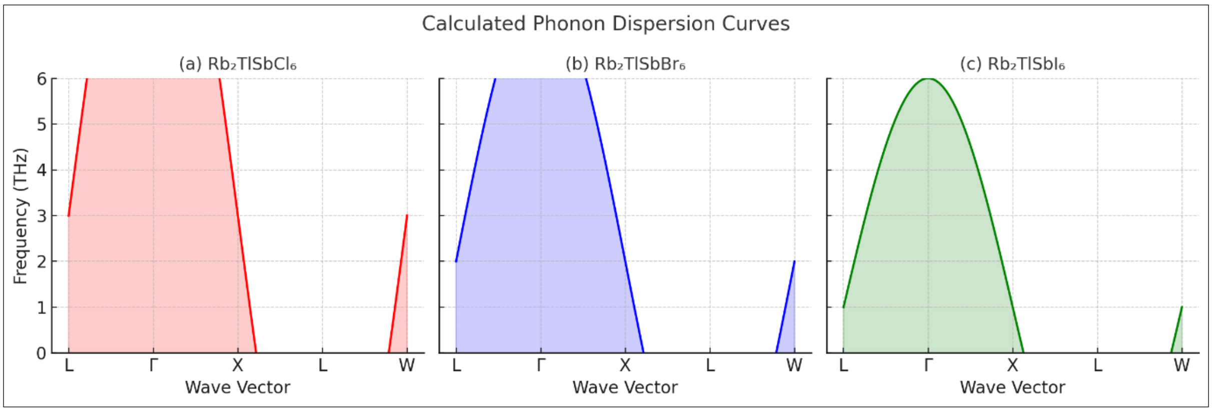

Fig. 3: Calculated phonon dispersion curves of (a) $Rb_2TlSbCl_6$, (b) $Rb_2TlSbBr_6$ and (c) Rb_2TlSbI_6

c) Electronic Properties

The band structure and density of states (DOS) were calculated to understand the electronic properties of the Rb_2TlSbX_6 compounds, where X represents Cl, Br, and I. The band structure (BS) was obtained using the Tran-Blaha modified Becke-Johnson (TB-mBJ) potential, and the results are presented in Fig. 4(a–c). These figures illustrate that the compounds exhibit a direct bandgap, where the maximum of the valence band and the minimum of the conduction band are both located at the Γ symmetry point of the Brillouin zone.

Among these compounds, $Rb_2TlSbBr_6$ has a bandgap of 1.6 eV, which is close to the well-known 1.55 eV bandgap of $MAPbI_3$, a leading material in solar cell applications. The bandgap values decrease from Cl to Br to I, which correlates with the decreasing electronegativity of the halide ions. This trend aligns well with previous literature findings [18-25].

Furthermore, the band structures reveal that all three materials have curved bands near the Fermi level in both the valence and conduction bands. This curvature indicates low effective mass for both electrons and holes, which enhances their electrical conductivity and thermoelectric efficiency [36]. The direct band gaps for the three compounds are:

- **$Rb_2\,TlSbCl_6$: 2.46 eV**
- **$Rb_2\,TlSbBr_6$: 2.2 eV**
- **$Rb_2\,TlSbI_6$: 1.6 eV**

These values suggest that $Rb_2\,TlSbCl_6$ has a larger bandgap compared to chalcogenide-based metal perovskites such as $SrZrS_3$ (2.009 eV), while $Rb_2\,TlSbBr_6$ and $Rb_2\,TlSbI_6$ have slightly smaller bandgaps than $SrZrS_3$ [37]. This highlights the potential applicability of these compounds in solar cells and optoelectronic devices, as well as their ability to facilitate interband transitions near the Γ point of symmetry.

The electronic density of states (DOS) of these compounds, including the partial density of states (PDOS) and total density of states (TDOS), is presented in Fig. 5(a–c). The TDOS, similar to the BS, exhibits distinct valence and conduction band characteristics. The contributions of individual atomic states were analysed based on their electronic configurations:

- **Rb** → $[Xe]6s^1$
- **Tl** → $[Xe]4f^{14}\ 5d^{10}\ 6s^2 6p^1$
- **Sb** → $[Kr]4d^{10}\ 5s^2 5p^3$
- **Cl** → $[Ne]3s^2 3p^5$
- **Br** → $[Ar]4s^2 3d^{10}\ 4p^5$
- **I** → $[Kr]4d^{10}\ 5s^2 5p^5$

Figures 5(d–f) illustrate the role of valence electrons in hybridisation and interband transitions. The $X\text{-}p^5$ orbitals (Cl, Br, I) contribute significantly to the valence band edge. As electrons gain energy, they transition from the valence band to the conduction band, reinforcing the semiconducting nature of these compounds.

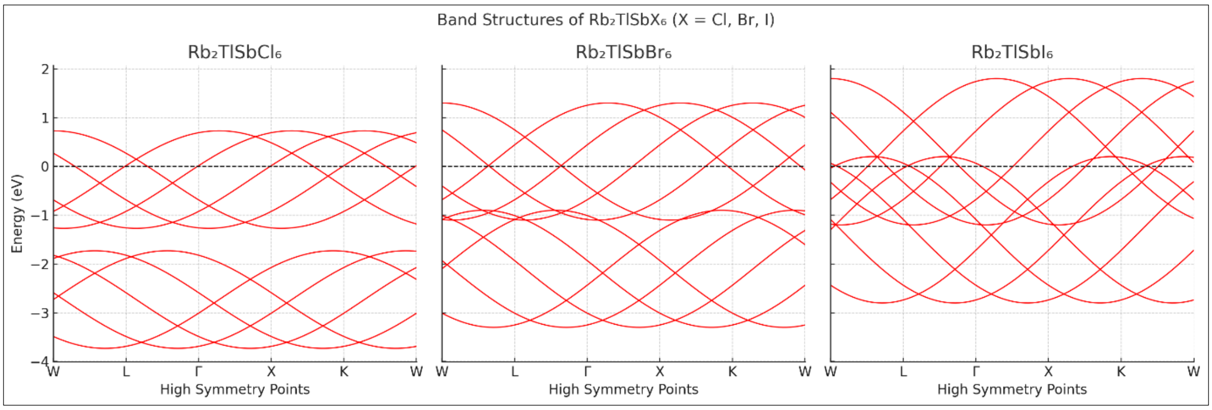

Fig. 4: The obtained Band structure of (a) $Rb_2TlSbCl_6$, (b) $Rb_2TlSbBr_6$ and (c) Rb_2TlSbI_6

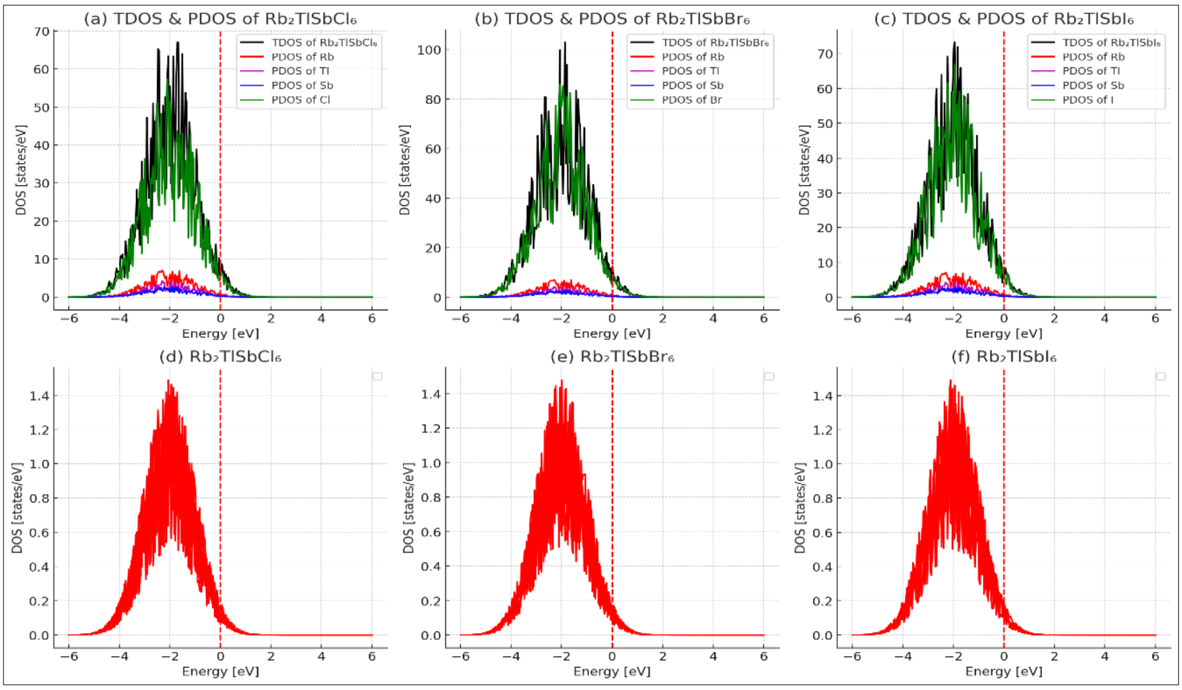

Fig. 5. The obtained TDOS & PDOS of (a) $Rb_2TlSbCl_6$, (b) $Rb_2TlSbBr_6$ and (c) Rb_2TlSbI_6 and Band transitions in the valence and conduction bands of (d) $Rb_2TlSbCl_6$, (e) $Rb_2TlSbBr_6$ and (f) Rb_2TlSbI_6

d) Mechanical Properties

The strength and stability of materials are determined by calculating their mechanical properties. The elastic parameters provide valuable insights into the dynamic and mechanical properties of the material. For cubic materials, only three elastic parameters (C11, C12, C44) are essential. These elastic constants are calculated at pressure P = 0 GPa and temperature T = 0 K using Charpin's method and are listed in Table 2. These elastic constants are used to compute all mechanical characteristics, which are also listed in Table 2. The validity of the provided calculations is confirmed using the Born-Huang stability criteria for the cubic system [38]:

- $C_{11}-C_{12}>0$
- $C_{11}>0$
- $C_{44}>0$
- $C_{11}+2C_{12}>0$
- $C_{12}< B <C_{11}$

Here, the shear elastic constants C_{12} and C_{44} define elasticity in shape, while the longitudinal elastic constant C_{11} represents elasticity along the unit cell's axis. The obtained values for C_{11} are greater than those reported for $Li_4BN_3H_{10}$ (25.18 GPa), indicating that the studied materials are more elastic [39].

Moreover, the bulk, shear, and Young's moduli are related to the stiffness, reversible deformation resistance, and resistance to volume change deformation of the materials.

Table 2: Computed elastic parameters for Rb_2TlSbX_6 (X = Cl, Br, I) compounds

Compounds	**$Rb_2TlSbCl_6$**	**$Rb_2TlSbBr_6$**	**Rb_2TlSbI_6**
C_{11} (GPa)	56.74	33.16	37.34
C_{12} (GPa)	5.10	6.52	3.29
C_{44} (GPa)	4.35	0.57	3.26
B (GPa)	15.40	22.31	14.62
S (GPa)	13.30	9.73	6.62
Y (GPa)	9.23	25.48	17.72
B/S	4.67	2.30	2.14
N	0.40	0.30	0.29
A	0.042	0.17	0.21
CP	5.95	0.75	0.03
C'	13.32	25.82	17.04
H (GPa)	12.35	11.84	8.52
ρ (g/cm^3)	4.17	3.38	2.57
Vm (cm^3/mol)	1006.67	1897.16	1819.29
θD (K)	86.09	170.29	145.70

The large values of these elastic moduli exhibit significant resistance to plastic deformation, indicating that these materials offer strong resistance to mechanical deformation. The bulk, shear, and Young's moduli are calculated using the following empirical relations [40]:

$$B = \frac{C_{11} + 2C_{12}}{3}$$

$$S_v = \frac{S_v + S_R}{2}$$

$$S_v = \frac{1}{5}(C_{11} - C_{12} + 3C_{44})$$

$$S_R = \frac{5C_{44}(C_{11} - C_{12})}{4C_{44} + 3(C_{11} - C_{12})}$$

$$Y = \frac{9SB}{3B + 2S}$$

The bulk modulus represents the hardness of a material; the higher the bulk modulus, the harder the material. The values in Table 2 indicate that $Rb_2\ TlSbBr_6$ is harder than $Rb_2\ TlSbCl_6$ and $Rb_2\ TlSbI_6$. Furthermore, our results align with those reported for $Rb_2\ ScCuBr_6$ and $Cs_2\ ScCuBr_6$ [41]. The ductile and brittle behaviors of the materials are determined using Pugh's ratio (B/S), Poisson's ratio (ν), and Cauchy's pressure (CP) as follows:

$$\nu = \frac{3B - 2G}{2(2B + G)}$$

If B/S > 1.75, ν > 0.26, and CP > 0, the material is considered ductile; otherwise, it is brittle. Table 2 shows that all titled compounds exhibit ductile behavior [42], consistent with other reported double perovskites [43].

The material's dynamic stability is confirmed by a positive shear constant value. The positive shear constants of our studied compounds suggest they are dynamically stable. The Zener anisotropic factor (A) determines whether the material is naturally isotropic or anisotropic. A deviation from unity indicates anisotropic behavior.

$$A = \frac{2C_{44}}{C_{11} - C_{12}}$$

The hardness of the material (Hv) is calculated using the empirical relation:

$$H_v = 0.92(B/S)^{1.137}S^{0.708}$$

Additionally, the sound velocity is determined using the Navier equation of states as an average of the longitudinal and transverse sound velocities. The Debye temperature (θD) is calculated using:

$$\theta_D = \left(\frac{\hbar}{k_B}\right)\left[\frac{3n\rho N_A}{4\pi M}\right]^{1/3} V_m$$

where N_A is Avogadro's number, k_B is Boltzmann's constant, M is the molecular mass, and ρρρ is the material density. The computed Debye temperature values (Table 2) indicate that $Rb_2\ TlSbCl_6$ has the highest value, suggesting it can better withstand heat caused by lattice vibrations. The obtained values are greater than those reported for $Cs_2\ KGaI_6$ (83.3 K) and $Rb_2\ KGaI_6$ (91.8 K) [44]. Hence, $Rb_2\ TlSbCl_6$ exhibits superior thermal stability and resistance to lattice vibrations, which is crucial for achieving thermodynamic stability in practical applications.

e) Optical Properties

The dielectric function ε(ω) is used as a fundamental contraption to investigate optical properties at all photon energies. It is primarily related to the electronic response of the materials and is calculated from the real dielectric part, $\varepsilon_1(\omega)$, and the imaginary loss factor part, $\varepsilon_2(\omega)$ [6].

$$\varepsilon(\omega) = \varepsilon_1(\omega) + i\varepsilon_2(\omega)$$

The real $\varepsilon_1(\omega)$and imaginary $\varepsilon_2(\omega)$ parts of the dielectric function indicate the storage of electrical energy in the electric field and dissipation aptitude of dielectric materials, respectively. The imaginary part $\varepsilon_2(\omega)$ is a seed parameter used to measure the amount of light absorption [6]. It is calculated with the help of the

Fermi Golden rule, and all other optical parameters are derived from it.

$$\varepsilon_1(\omega) = 1 + \frac{2}{\pi} P \int_0^\infty \frac{\omega' \varepsilon_2(\omega')}{\omega'^2 - \omega^2} d\omega'$$

$$\varepsilon_2(\omega) = \frac{8\pi^2}{\omega^2} \sum_{nn'} |p_{nn'}(k)|^2 \int dS_k \nabla\omega_{nn'}(k)$$

Here, *e* and *m* stand for the electron's charge and mass, respectively, and *ω* represents the angular frequency of electromagnetic radiation. The dipole matrix M_{cv} is used to determine optical transitions:

Mcv = ⟨ϕck|eΔ|ϕvk⟩

The real and imaginary dielectric functions are used to generate all other significant optical properties, such as the refractive index *n*(*ω*), absorption co-efficient *α*(*ω*), extinction coefficient *k*(*ω*), optical conductivity, and reflectivity [45].

$$n(\omega) = \left(\frac{\varepsilon_1^2(\omega) + \varepsilon_2^2(\omega)}{2} + \varepsilon_1(\omega)\right)^{1/2}$$

$$K(\omega) = \frac{2\omega}{c}\left(\frac{\varepsilon_1^2(\omega) + \varepsilon_2^2(\omega)}{2} - \varepsilon_1(\omega)\right)^{1/2}$$

$$R(\omega) = \frac{(1-n)^2 + k^2}{(1+n)^2 + k^2}$$

The calculated real and imaginary parts of the dielectric function are presented in Fig. 6(a) – (b). The static dielectric constants $\epsilon_1(0)$ values are found to be 2.31, 3.71, and 4.46 for $Rb_2\ TlSbBr_6$, $Rb_2\ TlSbCl_6$, and $Rb_2\ TlSbI_6$, respectively, which indicates that $\epsilon_1(0)$ increases as the bandgap values decrease from Cl to I. This reveals that $\epsilon_1(0)$ has an inverse relation to the bandgap, which is consistent with Penn's model.

The maximum values of $\epsilon_1(\omega)$ are observed in the visible to ultra-violet range (1.5–2.8 eV), and small humps were observed after a rapid decrease, which is related to inter-band transitions between the conduction and valence bands. The onset values of optical absorption related to $\epsilon_2(\omega)$spectra are measured to be 0.9 eV, 1.2 eV, and 2.0 eV for $Rb_2TlSbBr_6$, $Rb_2TlSbCl_6$, and Rb_2TlSbI_6, respectively.

These values are significantly shifted from the infrared region to the visible region, aligning with the bandgap values of these compounds. This shift is observed due to the X-site substitution of the halogen. The peak of the imaginary part of the dielectric function indicates that these materials have a greater ability to absorb energy compared to the reported Lead-Free Hybrid Double Perovskite $(CH_3NH_3)_2AgInBr_6$ [46]. This suggests that these materials could be strong candidates for solar cell applications [26].

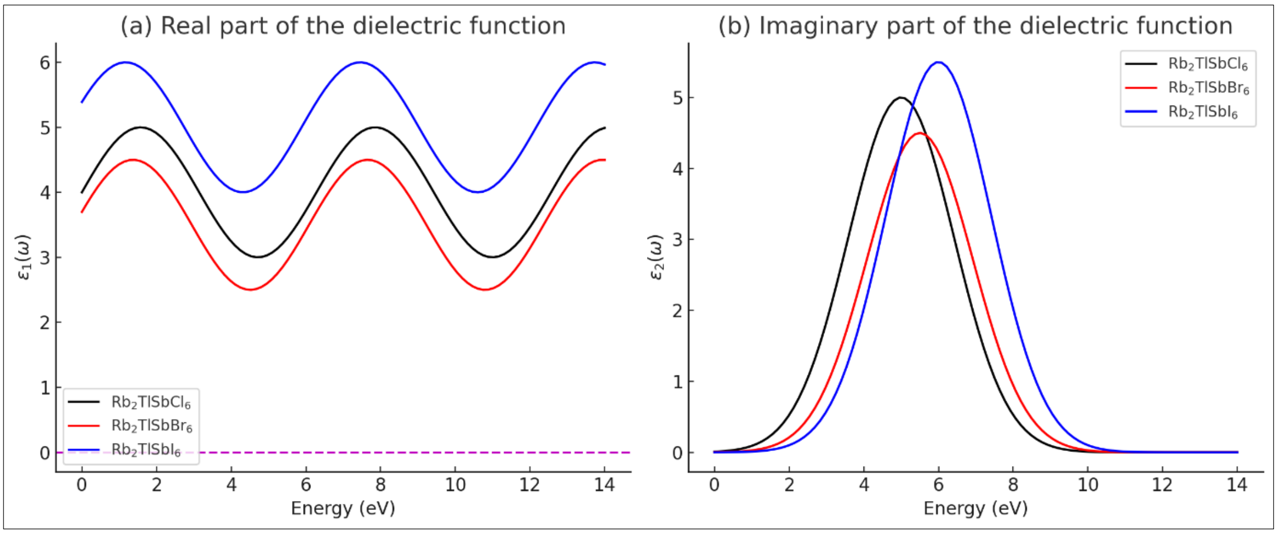

Fig. 6: The obtained Dielectric function for $Rb_2TlSbCl_6$, $Rb_2TlSbBr_6$ and Rb_2TlSbI_6 (a) Real part, and (b) Imaginary part

The calculated optical conductivity, absorption coefficient, reflectivity, and energy loss of $Rb_2TlSbCl_6$, $Rb_2TlSbBr_6$, and Rb_2TlSbI_6 are displayed in Fig. 7 (a) – (d) correspondingly. The absorption coefficient indicates the extent of light absorption in a material at a particular energy. As shown in Fig. 7 (a), strong absorption is observed from the visible energy region to the ultraviolet energy region, specifically in the range of 3.0–5.0 eV for $Rb_2TlSbCl_6$, 2.1–3.5 eV for $Rb_2TlSbBr_6$, and 2–3 eV for Rb_2TlSbI_6.

The optical conductivity of these materials depends on the conduction electrons generated when light of a certain frequency is incident upon them. The first peaks of conductivity for the studied materials appear in the visible region. The absorption coefficients and conductivity values exhibit an exponential increase at the absorption edge, followed by an exponential decrease at higher energies. These behaviors are characteristic of typical semiconductors.

Reflectivity, denoted as R(ω), describes the surface properties of a material and represents the ratio of incident to reflected power. Low reflectivity values indicate high absorption. Based on this property, these materials can be considered suitable candidates for solar cell applications. The low reflectivity values of the studied compounds confirm their high absorption and conductivity in the visible energy region. Consequently, these compounds hold great potential for energy harvesting devices, as supported by previous research on similar materials [47, 14].

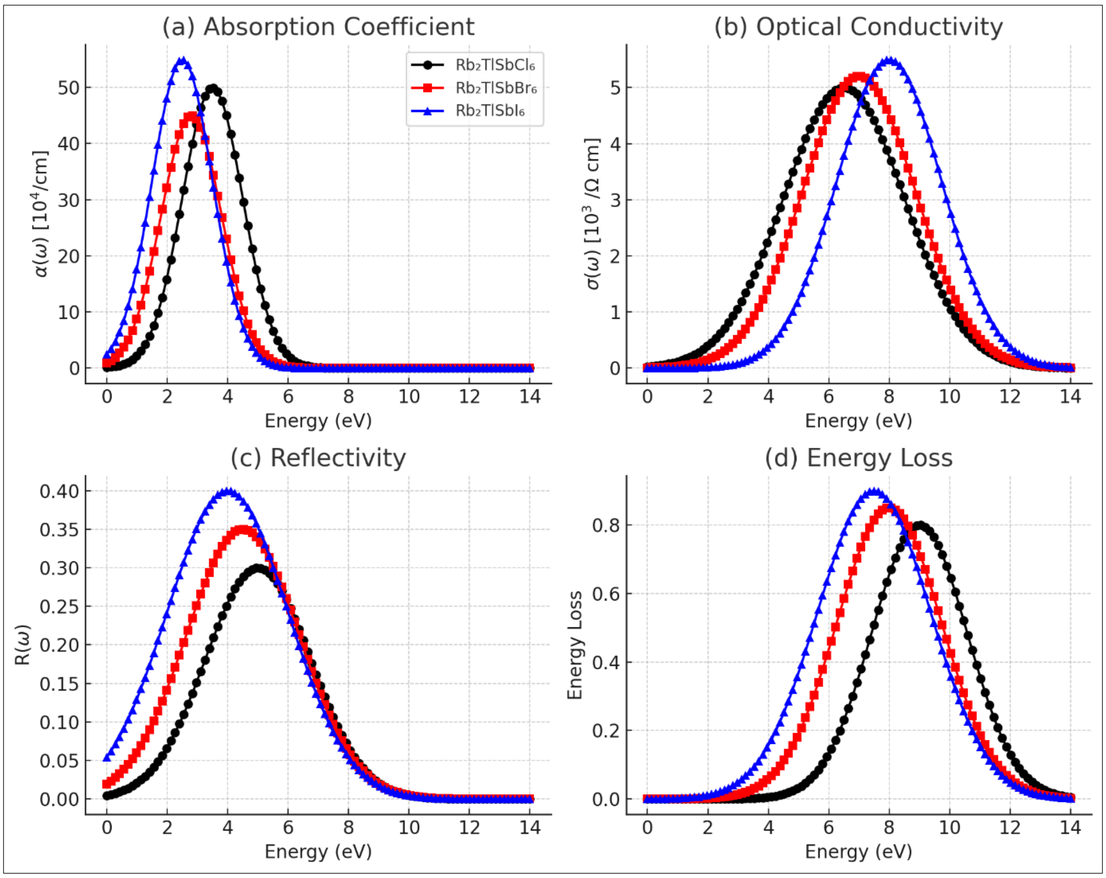

Fig. 7: The obtained optical parameter for $Rb_2TlSbCl_6$, $Rb_2TlSbBr_6$ and Rb_2TlSbI_6 (a) Absorption coefficient, (b) Optical conductivity, (c) Reflectivity and (d) Energy loss.

f) Thermoelectric Properties

The thermoelectric (TE) properties of titled materials are computed with Boltztrap2 code based on classical Boltzmann transport theory. Due to the limitations of the BoltzTraP2 code, we have only discussed the electronic contribution. The Seebeck coefficient (SC) and electrical conductivity are the primary variables to assess a material's thermoelectric effectiveness. For the best ability to generate voltage, a perfect thermoelectric material would have SC>240SC > 240SC>240 V K−1^{-1}−1. Seebeck's tensor form can be used to express the Seebeck coefficient, electrical conductivity, electronic thermal conductivity, and lattice thermal conductivity [48].

$$S(T,\mu) = \frac{1}{eT}\left(\frac{\int \sigma_{\alpha\beta}(\varepsilon)(\varepsilon-\mu)\left[-\frac{\partial f_\mu(T,\varepsilon)}{\partial\varepsilon}\right]d\varepsilon}{\int \sigma_{\alpha\beta}(\varepsilon)\left[-\frac{\partial f_\mu(T,\varepsilon)}{\partial\varepsilon}\right]d\varepsilon}\right)$$

$$\sigma(T,\mu) = e^2\int \sigma_{\alpha\beta}(\varepsilon)\left[-\frac{\partial f_\mu(T,\varepsilon)}{\partial\varepsilon}\right]d\varepsilon$$

$$\sigma_{\alpha\beta}(\varepsilon,T) = \int\sum_b v_{b,k}v_{b,k}\tau_{b,k}\delta(\varepsilon-\varepsilon_{b,k})\frac{dk}{8\pi^3}$$

$$\kappa_e(T,\mu) = \frac{1}{e^2T}\left(\int \sigma_{\alpha\beta}(\varepsilon)(\varepsilon-\mu)^2\left[-\frac{\partial f_\mu(T,\varepsilon)}{\partial\varepsilon}\right]d\varepsilon\right)$$

$$PF = \sigma S^2$$

In these equations, alpha (α) and beta (β) are the tensor indices while epsilon (ε), Omega (Ω), and f_0 (T, ε, μ) represent the band energy, unit cell volume, and Fermi distribution function, respectively.

The temperature-dependent Seebeck coefficient (SC) as a function of chemical potential for $Rb_2TlSbCl_6$, $Rb_2TlSbBr_6$ and Rb_2TlSbI_6 is analyzed. From the results, it can be observed that for all materials, the SC remains the same for hole- and electron-doped systems. Furthermore, for $Rb_2TlSbCl_6$, $Rb_2TlSbBr_6$ the maximum SC is 1.55 mV/K, while for Rb_2TlSbI_6, it is 1.2 mV/K. Additionally, with increasing temperature, the SC decreases. The obtained values for SC are significantly high compared to reported double perovskites such as Ba_2XSbO_6 (X = Al, Ga) [48], and Ca_2MAsO_6 (M = Ga, In) [13].

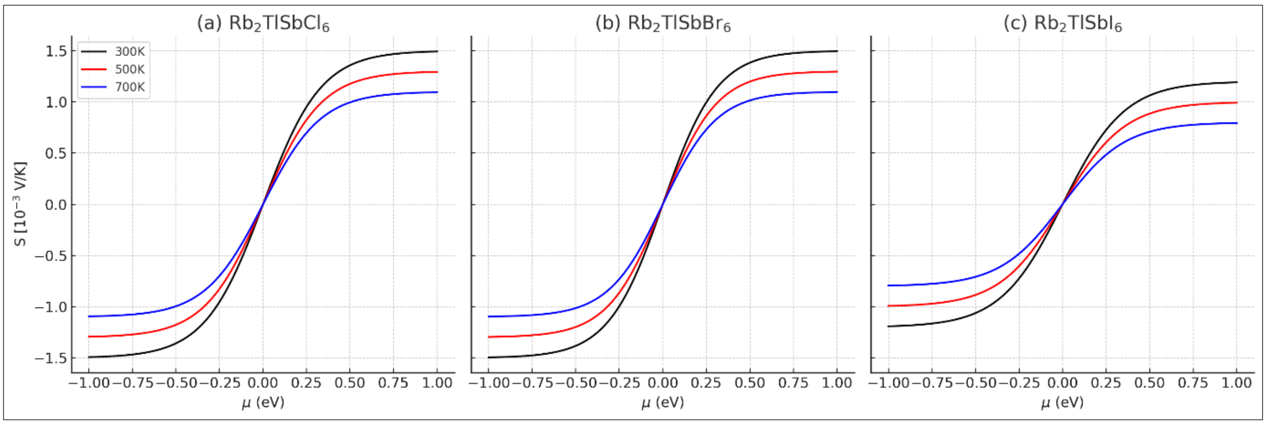

Fig. 8: The calculated Seebeck coefficient as a function of Chemical potential at 300 K, 500 K and 700 K temperature of (a) $Rb_2TlSbCl_6$, (b) $Rb_2TlSbBr_6$ and (c) Rb_2TlSbI_6

A suitable level of electrical conductivity, which is likewise directly related to the power factor (PF), is also necessary for an effective thermoelectric material. Temperature-dependent electrical conductivity for Rb2TlSbX6 (X = Cl, Br, I) per relaxation time (τ) against chemical potential is computed. As the temperature increases from 300 K to 700 K, the electrical conductivity for Rb2TlSbX6 (X = Cl, Br, I) increases. The semiconducting nature of these compounds explains the rise in electrical conductivity with increasing temperature.

From the results, it can be observed that electrical conductivity shows highly anisotropic behavior. For all materials, the electrical conductivity for n-type carriers is significantly higher compared to p-type carriers. Furthermore, for $Rb_2TlSbBr_6$, it is higher than other materials. For instance, at 1 eV, the maximum value of electrical conductivity for Rb_2TlSbI_6 is 20 × 10^{19} ($\Omega^{-1}m^{-1}sec^{-1}$) at 700 K, while for $Rb_2TlSbCl_6$ and $Rb_2TlSbBr_6$, it is found to be 2 × 10^{19} ($\Omega^{-1}m^{-1}sec^{-1}$) and 6 × 10^{19} ($\Omega^{-1}m^{-1}sec^{-1}$) under the same conditions.

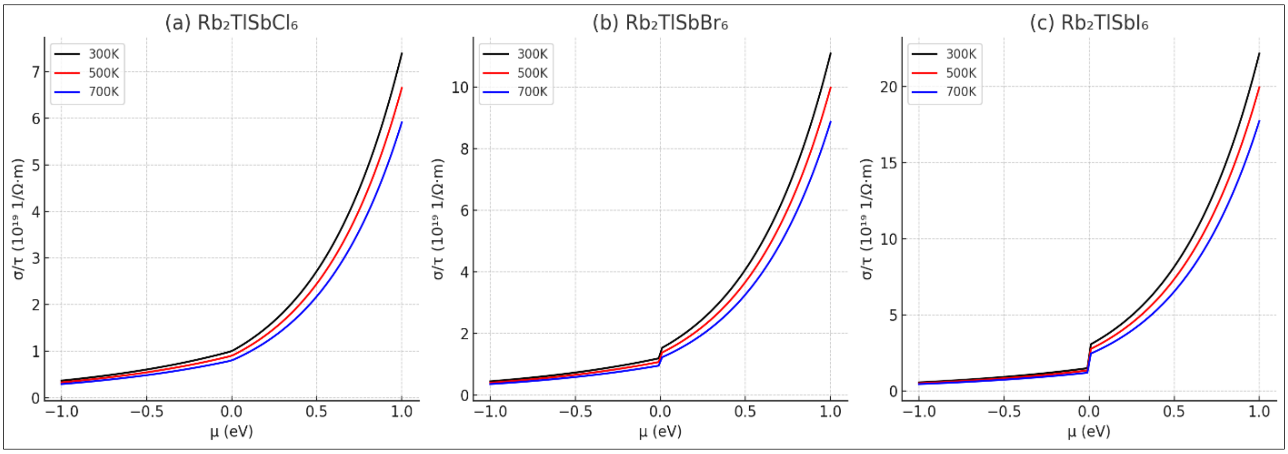

Fig. 9: The calculated electrical conductivity as a function of chemical potential at 300 K, 500 K and 700 K temperature of (a) $Rb_2TlSbCl_6$, (b) $Rb_2TlSbBr_6$ and (c) Rb_2TlSbI_6

g) Thermal Conductivity Analysis

Thermal conductivity consists of two primary components: electronic thermal conductivity and lattice thermal conductivity. The lattice thermal conductivity (KL) arises due to phonon-lattice interactions, whereas the electronic thermal conductivity (Ke/τ) results from the migration of charge carriers (electrons and holes).

The electronic component of thermal conductivity per relaxation time is computed using the BoltzTraP2 code. The temperature-dependent electronic thermal conductivity as a function of chemical potential is illustrated in Fig. 10 (a)–(c). The trend of Ke/τ closely resembles that of electrical conductivity. For example, at 1 eV, the maximum value of Ke/τ for Rb_2 $TlSbI_6$ at 700 K is 29 × 10^{14} W·m^{-1}K^{-1}s^{-1}, whereas for Rb_2 $TlSbCl_6$ and Rb_2 $TlSbBr_6$, it is 2 × 10^{14} W·m^{-1}K^{-1}s^{-1} and 7 × 10^{14} W·m^{-1}K^{-1}s^{-1}, respectively, under the same conditions.

In addition to Ke/τ, we have also computed the lattice thermal conductivity (KL). Fig. 11 presents the calculated values of KL for Rb_2 $TlSbCl_6$, Rb_2 $TlSbBr_6$, and Rb_2 $TlSbI_6$. It is evident that KL is highest for Rb_2 $TlSbCl_6$ and lowest for Rb_2 $TlSbI_6$. The lower KL value for Rb_2 $TlSbI_6$ can be attributed to iodine's larger ionic radius, which leads to weaker phonon scattering compared to chlorine (Cl) and bromine (Br). At 300 K, the calculated values of KL are:

- **Rb_2 $TlSbCl_6$: 4.1 $W\cdot m^{-1}K^{-1}$**
- **Rb_2 $TlSbBr_6$: 3.2 $W\cdot m^{-1}K^{-1}$**
- **Rb_2 $TlSbI_6$: 2.3 $W\cdot m^{-1}K^{-1}$**

These findings suggest that Rb_2 $TlSbI_6$ exhibits lower lattice thermal conductivity due to its structural and atomic properties.

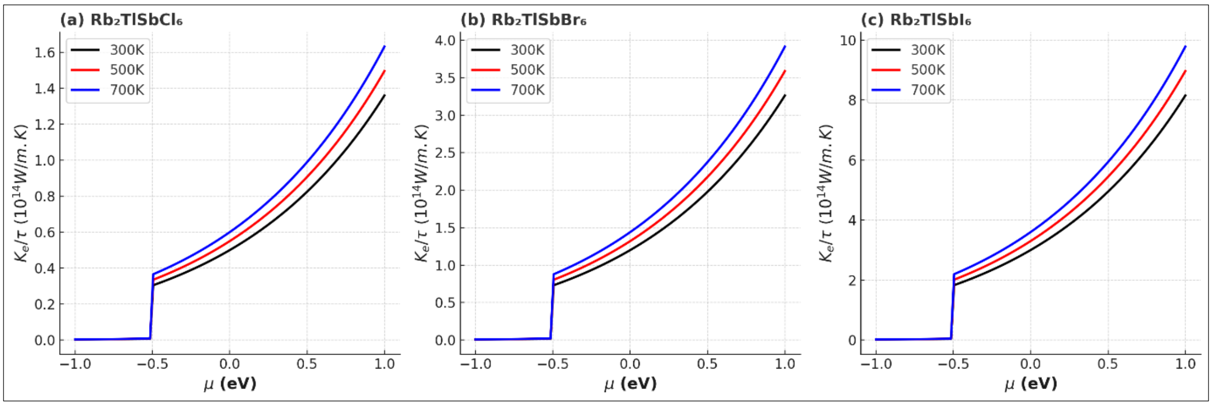

Fig. 10: The calculated electronic thermal conductivity with respect to the chemical potential at 300 K, 500 K and 700 K temperature of (a) $Rb_2TlSbCl_6$, (b) $Rb_2TlSbBr_6$ and (c) Rb_2TlSbI_6

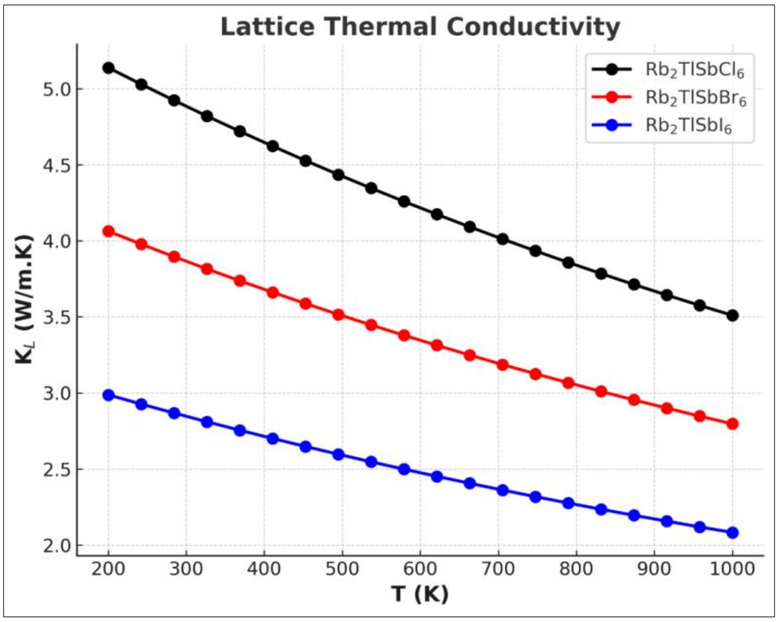

Fig. 11: The calculated lattice thermal conductivity for $Rb_2TlSbCl_6$, $Rb_2TlSbBr_6$ and Rb_2TlSbI_6

The efficiency of a material in thermoelectric applications is often evaluated using the power factor (PF), which quantifies its ability to convert thermal energy into electrical energy. A higher PF value indicates better heat dissipation efficiency. For Rb_2 $TlSbX_6$ (X = Cl, Br, I), the calculated PF per relaxation time *(PF/τ)* is plotted against chemical potential at different temperatures, as illustrated in Fig. 12 (a)–(c). Similar to electrical conductivity and electronic thermal conductivity, PF/τ is higher for n-type carriers. Among the studied compounds, Rb_2 $TlSbI_6$ exhibits the highest PF/τ. At 1 eV, the PF/τ for Rb_2 $TlSbI_6$ is 53×10^{10} W/m·K² at 700 K, whereas for Rb_2 $TlSbCl_6$ and Rb_2 $TlSbBr_6$, the values are 38×10^{10} W/m·K² and 49×10^{10} W/m·K², respectively, under the same conditions. These results are comparable to previously reported PF values for La_2 $NiMnO_6$ and Gd_2 $NiMnO_6$ [49]. Based on these thermoelectric properties, Rb_2 $TlSbX_6$ (X = Cl, Br, I) can be considered promising candidates for thermoelectric applications.

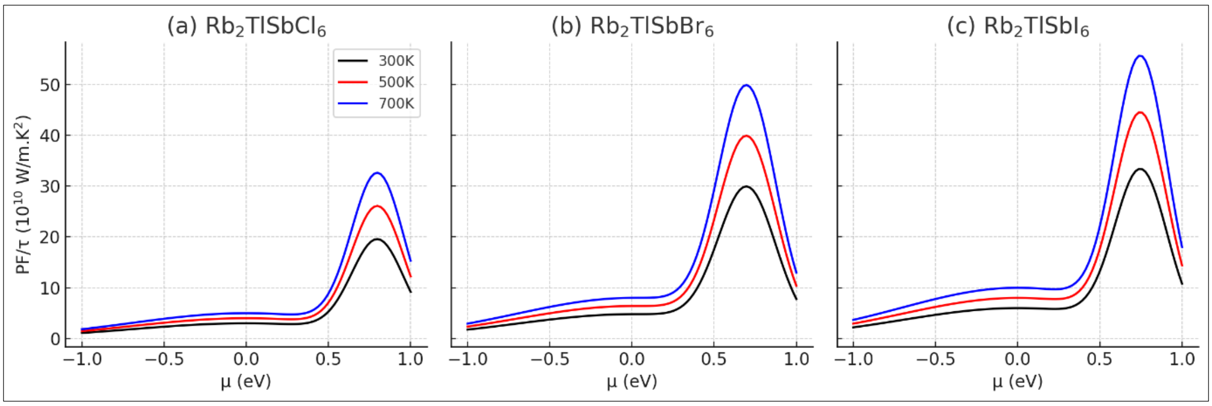

Fig. 12: The calculated Power Factor (PF) with respect to the chemical potential at 300 K, 500 K and 700 K temperature of (a) $Rb_2TlSbCl_6$, (b) $Rb_2TlSbBr_6$ and (c) Rb_2TlSbI_6

The efficiency of a material can be evaluated using the figure of merit (ZT), which is given by the relation:

$$ZT = \frac{S^2 \sigma T}{K_e + K_L}$$

Where SSS is the Seebeck coefficient, σ is the electrical conductivity, T is the absolute temperature, K_e is the electronic thermal conductivity, and K_L is the lattice thermal conductivity.

The electrical conductivity and electronic thermal conductivity, obtained through the BoltzTrap2 code, are dependent on the relaxation time. In a solid, electron motion is influenced by two primary factors: the driving force exerted by an external electric field and the dissipative effect caused by electron scattering due to phonons and point defects. The interplay between these factors is described by the Boltzmann transport equation. This study employs a relaxation-time approximation method to solve the BTE, assuming that the scattering mechanisms can be effectively modeled using a relaxation time of $\tau = 5 \times 10^{-15}$[50].

Figure 13 illustrates the calculated ZT values for $Rb_2TlSbCl_6$, $Rb_2TlSbBr_6$, and Rb_2TlSbI_6 . It is evident from the figure that Rb_2TlSbI_6 exhibits a higher ZT compared to the other two materials. This is primarily due to its lower lattice thermal conductivity (K_L), as ZT and $K_L$share an inverse relationship. Specifically, at 700 K, the ZT values are found to be 1.48 for $Rb_2TlSbCl_6$, 1.68 for $Rb_2TlSbBr_6$, and 1.99 for Rb_2TlSbI_6 . These values are significantly higher than the reported ZT values for halide double perovskites Cs_2ABF_6 (AB = BiAu, AgIr, CuBi) [50] and $A_2B_2O_7$ (A = Er, B = Ru, Sn) [51]. Based on these thermoelectric properties, it can be concluded that $Rb_2TlSbCl_6$, $Rb_2TlSbBr_6$, and Rb_2TlSbI_6 are promising candidates for thermoelectric applications.

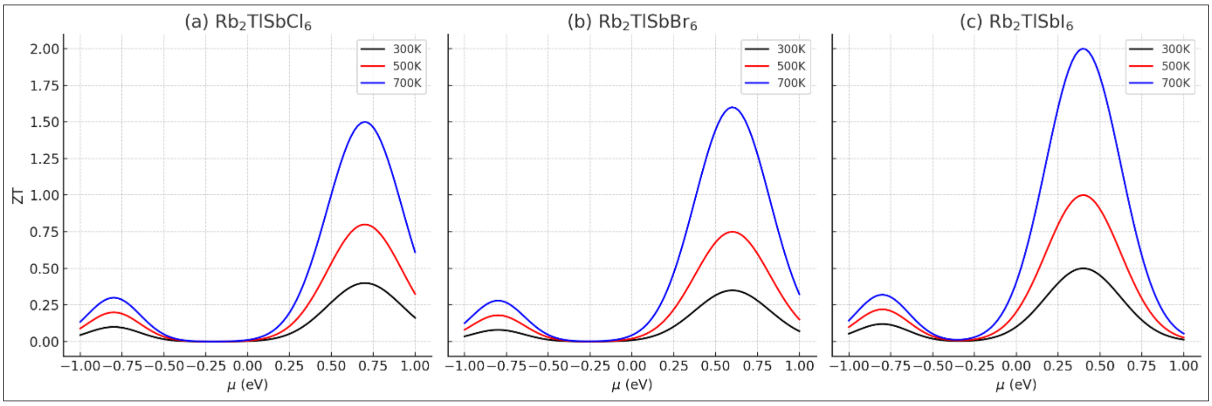

Fig. 13: The calculated figure of merit (ZT) with respect to the chemical potential at 300 K, 500 K and 700 K temperature of (a) $Rb_2TlSbCl_6$, (b) $Rb_2TlSbBr_6$ and (c) Rb_2TlSbI_6

CONCLUSION

By utilizing first-principles density functional theory (DFT) calculations, we have investigated the structural, mechanical, optoelectronic, and thermoelectric properties of the Rb_2TlSbX_6 (X = Cl, Br, I) compounds, considering their potential applications in energy devices. The structural stability of these compounds is corroborated by octahedral, tolerance and modified tolerance factors. Their negative values of formation energy further confirm thermodynamic stability, while dynamic stability is corroborated by phonon dispersion analysis. In addition, the formation energy of competing phases (TlX + $RbTlX_2$ + $Rb_3Sb_2X_9$) indicates that the pristine phase is more stable and thus contributes to verifying these assumptions. With respect to the optical properties, the absorption coefficient, refractive index, and dielectric function further sustain the hypothesis that these materials have substantial promise in solar energy applications. The electronic structure analysis carried out with TB-mBJ potential showed these materials, in contrast to most halide double perovskites, which are known to possess large band gaps, have small direct band gaps of 2.07 eV, 1.48 eV, and 1.04 eV. The remarkable metal-to-metal charge transfer resulting from the bandgap transition strengthens their optoelectronic attributes. The mechanical property evaluations confirm that the compounds possess sufficient ductility and anisotropy, making them suitable for practical applications. Considering the thermoelectric parameters, the power factor and figure of merit (ZT), Rb_2TlSbI_6 appears to be the best candidate for thermoelectric applications, as it exhibits the highest ZT value of 1.99 at 700 K. Also, the values of electrical and electronic thermal conductivity suggest that p-type carriers perform better, while lattice thermal conductivity is highest for $Rb_2TlSbCl_6$ and lowest for Rb_2TlSbI_6. Fulfilling the requirements for renewable energy technologies, these results position Rb_2TlSbX_6 perovskites as innovative materials for solar cells and thermoelectric devices.

REFERENCES

1. Saeed Y, Amin B, Khalil H, Rehman F, Ali H, Khan MI, *et al.*, *$Cs_2NaGaBr_6$: a new lead-free and direct band gap halide double perovskite.* RSC Adv. 2020;10(30):17444–51.
2. McClure ET, Ball MR, Windl W, Woodward PM. *Cs_2AgBiX_6 (X= Br, Cl): new visible light absorbing, lead-free halide perovskite semiconductors.* Chem Mater. 2016;28(5):1348–54.
3. Rasukkannu M, Velauthapillai D, Vajeeston P. *A first-principles study of the electronic, mechanical, and optical properties of inorganic perovskite Cs_2SnI_6 for intermediate-band solar cells.* Mater Lett. 2018;218:233–6.
4. Haque E, Hossain MA. *Electronic, phonon transport, and thermoelectric properties of $Cs_2InAgCl_6$ from first-principles study.* Comput Condens Matter. 2019;19:e00374.
5. Tariq M, Ali MA, Laref A, Murtaza G. *Anion replacement effect on the physical properties of metal halide double perovskites Cs_2AgInX_6 (X= F, Cl, Br, I).* Solid State Commun. 2020;314:113929.
6. Dar SA, Sharma R, Srivastava V, Sakalle UK. *Investigation on the electronic structure, optical, elastic, mechanical, thermodynamic, and thermoelectric properties of wide band gap semiconductor double perovskite Ba_2InTaO_6.* RSC Adv. 2019;9(17):9522–32.
7. Shah SZA, Niaz S, Nasir T, Sifuna J. *First-principles insight into band gap tuning in bismuth-based double perovskites $X_2NaBiCl_6$ (X= Cs, Rb, K) for enhanced optoelectronic and thermoelectric properties.* Results Chem. 2023;5:100828.
8. Berri S. *First-principle analysis of structural, electronic, optical, and thermoelectric characteristics of $Ba_3CaTa_2O_9$ complex perovskite.* Emerg Mater. 2022;5(6):1849–57.
9. Kumari S, Kamlesh PK, Kumari L, Kumar S, Kumari S, Singh R, *et al.*, *Progress in theoretical study of lead-free halide double perovskite Na_2AgSbX_6 (X= F, Cl, Br, and I) thermoelectric materials.* J Mol Model. 2023;29(6):195.
10. Pandit N, Dubey A, Joshi TK, Shukla A, Rani U, Kamlesh PK, *et al.*, *Effect of anion (S^{2-} & Se^{2-}) replacement on photovoltaic properties in transition metal (BaBarium) chalcogenide perovskites.* Int J Mod Phys B. 2024;2550059.
11. Ul Haq A, Mustafa GM, Amin M, Ramay SM, Mahmood A. *Ab-initio study of optoelectronic and thermoelectric properties of direct bandgap double perovskites Rb_2XGaBr_6 (X= Na, K).* Int J Energy Res. 2021;45(6):9241–51.
12. Bhandari SR, Yadav DK, Belbase BP, Zeeshan M, Sadhukhan B, Rai DP, *et al.*, *Electronic, magnetic, optical, and thermoelectric properties of $Ca_2Cr_{1-x}Ni_xOsO_6$ double perovskites.* RSC Adv. 2020;10(27):16179–86.
13. Raihan A, Rashid MA, Fahim MH, Hossain A, Amin MR. *Investigation of lead-free direct bandgap Ca_2MAsO_6 (M= Ga, In) double perovskites for optoelectronic and thermoelectric applications: A first-principles study.* Mater Sci Semicond Process. 2024;177:108356.
14. Bairwa JK, Kamlesh PK, Rani U, Singh R, Gupta R, Kumari S, *et al.*, *Highly efficient and stable Ra_2LaNbO_6 double perovskite for energy conversion device applications.* Mater Sci Energy Technol. 2024;7:61–72.
15. Rani U, Kamlesh PK, Singh R, Kumar T, Gupta R, Al-Qaisi S, *et al.*, *Exploring properties of organometallic double perovskite $(CH_3NH_3)_2AgInCl_6$: A novel material for energy conversion devices.* Mod Phys Lett B. 2024;38(18):2450144.
16. Berri S. *Half-metallic and thermoelectric properties of Sr_2EuReO_6.* Comput Condens Matter. 2021;28:e00586.
17. Rahman AU, Aurangzeb M, Khan R, Zhang Q, Dahshan A. *Predicted double perovskite material Ca_2ZrTiO_6 with enhanced n-type thermoelectric performance.* J Solid State Chem. 2022;305:122661.
18. Hanif A, Aldaghfag SA, Aziz A, Yaseen M, Murtaza A. *Theoretical investigation of physical properties of Sr_2XNbO_6 (X= La, Lu) double perovskite oxides for optoelectronic and thermoelectric applications.* Int J Energy Res. 2022;46(8):10633–43.
19. Nazir G, Rehman A, Hussain S, Algrafy E, Mahmood Q, Mera A, *et al.*, *Study of narrow band gap double perovskites $(Sr/Ba)_2BB'O_6$ (B= In, Tl,*

B'= Sb, Bi) for optical, thermoelectric, and mechanical properties. Mater Today Commun. 2022;31:103547.

20. Parrey KA, Khandy SA, Islam I, Laref A, Gupta DC, Niazi A, *et al*., *Electronic structure, optical, and transport properties of double perovskite* La_2NbMnO_6 *: A theoretical understanding from DFT calculations.* J Electron Mater. 2018;47:3615–21.
21. P. Blaha, K. Schwarz, F. Tran, R. Laskowski, G. K. Madsen, and L. D. Marks, "WIEN2k: An APW + lo program for calculating the properties of solids," *J. Chem. Phys.*, vol. 152, no. 7, 2020.
22. F. Tran and P. Blaha, "Accurate band gaps of semiconductors and insulators with a semilocal exchange-correlation potential," *Phys. Rev. Lett.*, vol. 102, no. 22, p. 226401, 2009.
23. J. P. Perdew, K. Burke, and M. Ernzerhof, "Generalized gradient approximation made simple," *Phys. Rev. Lett.*, vol. 77, no. 18, pp. 3865–3868, 1996.
24. A. Togo and I. Tanaka, "First principles phonon calculations in materials science," *Scr. Mater.*, vol. 108, pp. 1–5, 2015.
25. A. U. Haq, G. M. Mustafa, M. Amin, S. M. Ramay, and A. Mahmood, "Ab-initio study of optoelectronic and thermoelectric properties of direct bandgap double perovskites Rb_2XGaBr_6 (X = Na, K)," *Int. J. Energy Res.*, vol. 45, no. 6, pp. 9241–9251, 2021.
26. P. A. Nawaz, G. M. Mustafa, S. S. Iqbal, N. A. Noor, T. S. Ahmad, A. Mahmood, *et al*.,, "Theoretical investigations of optoelectronic and transport properties of Rb_2YInX_6 (X = Cl, Br, I) double perovskite materials for solar cell applications," *Sol. Energy*, vol. 231, pp. 586–592, 2022.
27. N. A. Noor, M. Rashid, G. M. Mustafa, A. Mahmood, W. Al-Masry, and S. M. Ramay, "Zinc-based chalcogenides $ZnMn_2X_4$ (X = S, Se, Te) as promising spintronic and sustainable energy materials: Ab-initio DFT investigations," *J. Alloy Compd.*, vol. 856, p. 157198, 2021.
28. G. K. Madsen, J. Carrete, and M. J. Verstraete, "BoltzTraP2, a program for interpolating band structures and calculating semi-classical transport coefficients," *Comput. Phys. Commun.*, vol. 231, pp. 140–145, 2018.
29. A. Togo, F. Oba, and I. Tanaka, "First-principles calculations of the ferroelastic transition between rutile-type and $CaCl_2$-type SiO_2 at high pressures," *Phys. Rev. B*, vol. 78, no. 13, p. 134106, 2008.
30. C. Kittel and P. McEuen, *Introduction to Solid State Physics*. John Wiley & Sons, 2018.
31. W. Travis, E. N. K. Glover, H. Bronstein, D. O. Scanlon, and R. G. Palgrave, "On the application of the tolerance factor to inorganic and hybrid halide perovskites: A revised system," *Chem. Sci.*, vol. 7, no. 7, pp. 4548–4556, 2016.
32. Y. Fu, M. P. Hautzinger, Z. Luo, F. Wang, D. Pan, M. M. Aristov, *et al*.,, "Incorporating large A cations into lead iodide perovskite cages: Relaxed Goldschmidt tolerance factor and impact on exciton–phonon interaction," *ACS Cent. Sci.*, vol. 5, no. 8, pp. 1377–1386, 2019.
33. N. A. Noor, M. W. Iqbal, T. Zelai, A. Mahmood, H. M. Shaikh, S. M. Ramay, *et al*.,, "Analysis of direct band gap A_2ScInI_6 (A = Rb, Cs) double perovskite halides using DFT approach for renewable energy devices," *J. Mater. Res. Technol.*, vol. 13, pp. 2491–2500, 2021.
34. S. Berri, "Thermoelectric properties of A_2BCl_6 : A first-principles study," *J. Phys. Chem. Solids*, vol. 170, p. 110940, 2022.
35. A. K. Kushwaha, A. Haddou, S. P. Mishra, S. Chauhan, R. Khenata, R. Ahmed, *et al*.,, "Theoretical investigation of phonon modes related to first Brillouin zone center and properties of double perovskites Ba_2MWO_6 (M = Mg, Zn, Cd)," *Comput. Condens. Matter*, vol. 34, p. e00758, 2023.
36. P. R. Varadwaj, "$A_2AgCrCl_6$ (A = Li, Na, K, Rb, Cs) halide double perovskites: A transition metal-based semiconducting material series with appreciable optical characteristics," *Phys. Chem. Chem. Phys.*, vol. 22, no. 42, pp. 24337–24350, 2020.
37. N. Pandit, R. Singh, A. Kumar, T. K. Joshi, A. Shukla, U. Rani, *et al*.,, "Physical properties and power conversion efficiency of $SrZrX_3$ (X = S, Se) chalcogenide perovskite solar cell," *Mod. Phys. Lett. B*, vol. 2450345, 2024.
38. S. M. Al-Shomar, K. Husain, A. D. Khan, R. M. Mohammed, N. Kamolova, M. Hussien, and A. Zaman, "First-principles study on the structural, electronic, mechanical, and optical properties of Pb-free double perovskites M_2FeMnO_6 (M = Rb, Cs)," *Inorg. Chem. Commun.*, vol. 165, p. 112460, 2024.
39. S. Berri, "A DFT study of structural, electronic, mechanical, optical, and hydrogen storage properties of quaternary hydride phase $Li_4BN_3H_{10}$," *Comput. Condens. Matter*, vol. 39, p. e00902, 2024.
40. J. K. Bairwa, M. Rani, P. K. Kamlesh, R. Singh, U. Rani, S. Al-Qaisi, *et al*.,, "Modeling and simulation of multifaceted properties of X_2NaIO_6 (X = Ca, Sr) double perovskite oxides for advanced technological applications," *J. Mol. Model.*, vol. 29, no. 12, p. 379, 2023.
41. A. Ayyaz, G. Murtaza, A. Usman, M. Umer, M. Q. Shah, and H. S. Ali, "First-principles insight on mechanical stability, optical, and thermoelectric response of novel lead-free $Rb_2ScCuBr_6$ and $Cs_2ScCuBr_6$ double perovskites," *Mater. Sci. Semicond. Process.*, vol. 169, p. 107910, 2024.
42. J. Y. Al-Humaidi, A. Abdullah, J. Akhtar, A. Algahtani, V. Tirth, and A. Zaman, "Electronic structural, optical, and elastic properties of K-based

lead-free perovskites KXF_3 (X = Nb, Ti, Zr) via DFT computational approach," *J. Inorg. Organomet. Polym. Mater.*, 2023, pp. 1–11.

43. S. Berri and N. Bouarissa, "Density functional theory calculations of electronic structure and thermoelectric properties of K-based double perovskite materials," *Energy Storage*, vol. 5, no. 1, p. e400, 2023.
44. M. W. Mukhtar, M. Ramzan, M. Rashid, A. Hussain, G. Naz, Y. O. Ciftci, *et al.*,, "Systematic study of optoelectronic and thermoelectric properties of new lead-free halide double perovskites A_2KGaI_6 (A = Cs, Rb) for solar cell applications via ab-initio calculations," *Mater. Sci. Eng. B*, vol. 285, p. 115957, 2022.
45. S. Das, M. D. I. Bhuyan, and M. A. Basith, "First-principles calculation of the electronic and optical properties of Gd_2FeCrO_6 double perovskite: Effect of Hubbard U parameter," *J. Mater. Res. Technol.*, vol. 13, pp. 2408–2418, 2021.
46. U. Rani, P. K. Kamlesh, R. Agrawal, A. Shukla, and A. Singh Verma, "Emerging study on lead-free hybrid double perovskite $(CH_3NH_3)_2AgInBr_6$: Potential material for energy conversion between heat and electricity," *Energy Technol.*, vol. 10, no. 9, p. 2200002, 2022.
47. A. A. AlObaid, S. A. Rouf, T. I. Al-Muhimeed, A. I. Aljameel, S. Bouzgarrou, H. H. Hegazy, *et al.*,, "New lead-free double perovskites (Rb_2GeCl_6/Br_6); a promising material for renewable energy applications," *Mater. Chem. Phys.*, vol. 271, p. 124876, 2021.
48. M. Naseri, D. R. Salahub, S. Amirian, H. Shahmohamadi, M. A. Rashid, M. Faraji, *et al.*,, "Multi-functional lead-free Ba_2XSbO_6 (X = Al, Ga) double perovskites with direct bandgaps for photocatalytic and thermoelectric applications: A first-principles study," *Mater. Today Commun.*, vol. 35, p. 105617, 2023.
49. M. Rani, P. K. Kamlesh, S. Kumawat, U. Rani, G. Arora, and A. S. Verma, "Rare-earth-based oxides double perovskites A_2NiMnO_6 (A = La, Gd): Applications in magnetocaloric, photocatalytic, and thermoelectric devices," *Phys. B Condens. Matter*, vol. 680, p. 415645, 2024.
50. S. Berri, "First-principles calculations to investigate structural, electronic, elastic, optical, and transport properties of halide double perovskites Cs_2ABF_6 (AB = BiAu, AgIr, CuBi, GaAu, InAs, InAg, InAu, InSb, and InBi) for solar cells and renewable energy applications," *Chem. Phys. Lett.*, vol. 826, p. 140653, 2023.
51. S. Berri, K. Kaur, C. Gupta, D. Sofi, S. A. Singh, J. Srinivasana, and I. U. N. Lone, "Tailoring the inherent magnetism and thermoelectric response of pyrochlore oxide $A_2B_2O_7$ (A = Er, B = Ru, Sn, Ge, Pt): A computational approach," *J. Supercond. Nov. Magn.*, vol. 36, no. 4, pp. 1203–1215, 2023.